Initial Assessment of Space Launch System Transonic Unsteady Pressure Environment

Martin K. Sekula[*], David J. Piatak[†], Russ D. Rausch[‡], James R. Florance[§]
NASA Langley Research Center, Hampton, VA 23681

and

James M. Ramey[**]
Jacobs Technology, Inc., Hampton, VA 23681

A series of wind tunnel tests were conducted at the NASA Langley Research Center Transonic Dynamics Tunnel to assess the transonic buffet environment for the Space Launch System (SLS) launch vehicle. An initial test, conducted in 2012, indicated an elevated buffet environment prompting a second test to provide further insight into the buffet phenomena and assess potential solutions to reduce the response levels of these environments. During the course of the test program, eight variants of the SLS-10000 configuration were examined. The effect of these configuration variants on the coefficient of the root-mean-square fluctuation of pressure about the mean as a function of test condition indicates that the maximum fluctuating pressure levels are extremely sensitive to the geometry of the forward attachment of the solid rocket boosters (SRBs) to the SLS Core. The addition of flow fences or changes to the SRB nose cone geometry can alleviate the unsteady pressure environment.

Nomenclature

L_c = coherence length
M = Mach number
$\Delta C_{p,rms}$ = coefficient of the root-mean-square fluctuation of pressure about the mean
α = model pitch angle
ϕ = model roll angle

Notice to Readers

The predicted performance and certain other features and characteristics of the Space Launch System vehicle are defined by the U.S. Government to be Sensitive But Unclassified (SBU). Therefore, values in plots and figures have been either removed or normalized to arbitrary values.

I. Introduction

The buffet environment encountered by launch vehicles as they accelerate through the transonic range is a significant contributor to the definition of their structural design requirements. Between 2012 and 2014, two wind tunnel tests were conducted at the NASA Langley Transonic Dynamics Tunnel where highly-instrumented rigid buffet models (RBMs) were employed to assess the transonic buffet environment experienced by the Space Launch System (SLS) launch vehicle.[1]

The initial RBM test of the SLS launch vehicle occurred in the fall of 2012. One of the main goals of this test was to examine the buffet environment of the SLS-10003 configuration.[1] The initial buffet forcing functions (BFFs) developed from data acquired during this test identified high unsteady loads acting over an unusually wide range of

---

test conditions. While some analytical sources, such as surface pressure integration boundaries, were found to artificially elevate these high loads (and were addressed through updates to the BFF development methodology), the underlying cause was determined to be the solid rocket booster (SRB) forward attachment (FA) geometry. A series of experimental and analytical studies followed to examine the performance of various candidate buffet mitigation options (BMOs). After a down-select process during which the best performing BMOs were identified, a follow-on RBM test conducted in the spring of 2014 examined a configuration updated to the more current SLS-10005 geometry and potential BMOs.

The initial 2012 test acquired unsteady pressure data on the surface of the SLS vehicle using 360 miniature unsteady pressure transducers. These transducers were located at 35 longitudinal stations on the vehicle and grouped in rings of four, six, or eight transducers. During the second test, the model was modified to expand the transducer count to 472, providing three additional transducer stations and increasing the transducer density to either four, eight, or sixteen equidistant transducers at each station. Figure 1 provides the final transducer layout.

In addition to updating the feedlines, presslines, system tunnel, and other protuberances to the SLS-10005 outer mold line (OML), one of the major changes to the model was an update of the FA geometry. The model tested in 2012 featured a simplified FA geometry—a placeholder design. The 2014 model featured an updated, detailed FA geometry. These two FA geometries are presented in Fig. 2. A comparison of the effect of these two FA geometries on the fluctuating pressure environment will be presented.

The 2014 test also examined the effect of several BMOs on the fluctuating pressure environment. These BMOs can be divided into two categories: flow fences and SRB nose cones. The fences provide a low-cost solution to reduce the fluctuating pressures, but at a significant weight penalty. The nose cones, on the other hand, may require a high development cost to retrofit the boosters, but have a potential benefit of little or no additional weight. The three fence configurations, presented in Fig. 3, were installed in identical sets of four on either the SRBs or the Core near the SRB forward attachments in an effort to isolate the flow around and behind the FA from the shock-dominated flow environment that impinges on the sides of the Core and SRBs. Figure 4 presents the SRB nose cone BMOs. These nose cones were designed to reduce the fluctuating pressure environment in the vicinity and downstream of the SRB FA as well as at the SRB nose-cone/main-body shoulder.

II. Analysis

The unsteady aerodynamic environment encountered by the SLS launch vehicle is assessed using two metrics: the coefficient of the root-mean-square fluctuation of pressure about the mean (i.e., standard deviation) and coherence length. The first metric is the coefficient of the root-mean-square (rms) fluctuation of pressure about the mean, $\Delta C_{p,rms}$, calculated from measured pressure time histories at individual locations on the vehicle. $\Delta C_{p,rms}$ provides an assessment of the severity of the local fluctuating pressure environment. The two configurations of the SLS RBM wind tunnel model (SLS-10003 and SLS-10005) utilized hundreds of unsteady pressure transducers to assess the transonic buffet environment. A detailed examination of the individual pressure time histories for all transducers at all test conditions is not practical. Therefore, to provide an overview of the most important elements of the fluctuating pressure environment, the maximum $\Delta C_{p,rms}$ encountered anywhere on each of the three SLS components (Core, left SRB, and right SRB) are plotted as a function of wind-tunnel test condition. Figures 5(a)–(c) provides a sample set of color intensity plots presenting the maximum $\Delta C_{p,rms}$ as a function of Mach number and absolute model pitch angle for the simplified FA geometry. It should be noted, that the data are linearly interpolated between discrete test conditions at which they were acquired. Also, for each Mach-model pitch angle combination, it is possible that the value plotted may be the maximum value based on multiple data points, accounting for various model roll angles at a model pitch angle as well as repeat conditions.

To provide further insight into the maximum $\Delta C_{p,rms}$ plots, a supplemental set of plots, Figs. 6(a)–(c), color-identify the general location of the high buffet environment on the three components of the SLS vehicle. The SLS vehicle was divided into ten segments of interest: Launch Abort System (LAS), Multi-Purpose Crew Vehicle (MPCV), Interim Cryogenic Propulsion System (ICPS), ICPS-Core junction, interstage, SRB nose cones, SRB-nose-cone/main-SRB-body junction, FA region, aft Core/SRB region, and aft skirt. The locations of these regions are defined in the legend of Fig. 6. These ten regions are color coded, and therefore Fig. 6 indicates the general location of the transducer that measured the largest pressure fluctuations. Unlike Fig. 5, where data are linearly interpolated between discrete test conditions, these plots consist of a series of constant-value patches centered on the test conditions. This plotting approach was chosen since Fig. 6 represents a discontinuous function; i.e., the location of the maximum $\Delta C_{p,rms}$ can jump to different vehicle locations depending on the test condition. Therefore, linear interpolation can falsely indicate that a high fluctuating pressure measurement occurred at an intermediate region on the SLS vehicle.

The second metric is the coherence length, L_c, a measure of how quickly the structure of the flow changes. This quantity is determined in a multi-step approach.[2] First, the coherence of the pressure time histories is calculated between all permutations of transducer pairs in a selected region of the vehicle. The mean of the coherence over a buffet-specific frequency range is determined and plotted as a function of the separation distance between transducers. An exponential fit through the data is used to determine the separation distance at which the coherence reduces to a value of 0.5. This quantity is important since it is employed in the BFF generation process and helps determine the effective integration area associated with each transducer. Understanding how OML changes affect the coherence length provides insight into the buffet environment. For the purposes of this paper, L_c is determined for transducers highlighted with yellow boxes in Fig. 1. The unsteady aerodynamic environment in this region of the SLS Core was found to be heavily influenced by the SRB FA geometry.

Contour plots of the coherence length are presented in Fig. 7. A color intensity plot displays the maximum value of the coherence length as a function of flight condition. In the case of Fig. 7, L_c is presented as a function of Mach number and absolute model pitch angle for the two FA geometries. The color intensity indicates that the coherence length is extremely sensitive to Mach number and model pitch angle. As was the case with Fig. 5, each point on this plot may represent the maximum value based on several data points. Likewise, for each data point, L_c may be calculated at up to four azimuth angles around the Core: 45°, 135°, 225°, and 315°. Two of the four sets of the transducers employed in this analysis, are highlighted with yellow boxes in Fig. 1 (45° at the bottom, 315° at the top, whereas 135° and 225° are on the opposing side of the vehicle, not shown). Once the L_c is calculated for each set of transducers, the maximum of these lengths is determined and plotted.

III. Results

A. Effect of FA Geometry

The maximum $\Delta C_{p,rms}$ as a function of Mach number and absolute model pitch angle for the simplified forward attachment geometry (based on the 2012 test) is presented in Figs. 5(a)–(c), while Figs. 5(d)–(f) present the same data for the detailed forward attachment geometry tested in 2014. The figures indicate that the FA design caused a significant change in the $\Delta C_{p,rms}$ levels, which will be discussed in more detail below. The figures also indicate that the SLS Core is exposed to a much more severe fluctuating pressure environment than the two SRBs, and the highest $\Delta C_{p,rms}$ levels encountered by all three vehicle components occur in the Mach 0.9 to 0.95 range, regardless of the forward attachment geometry.

1. Core Fluctuating Pressures

The change in the FA geometry from simplified to detailed reduces the maximum $\Delta C_{p,rms}$ values on the Core and the Mach number band, where the $\Delta C_{p,rms}$ reaches a maximum value, narrows and shifts to a higher Mach number (compare Figs. 5(b) and (e), Mach 0.86–0.98 vs. Mach 0.92–0.96, respectively.) The Core location where the maximum $\Delta C_{p,rms}$ was identified always occurs behind the SRB forward attachments (See Figs. 6(b) and (e)), although this does not preclude other areas of potentially critical buffet environments. Figures 5(b) and (e) also indicate that between Mach 1 and 1.15 the detailed forward attachment geometry does increase the $\Delta C_{p,rms}$ levels at high model pitch angles (>4°), but this test condition is generally outside the typical pitch envelope for this vehicle.

Measured $\Delta C_{p,rms}$, mapped onto the vehicle OML, are presented in Fig. 8. These figures are for an attitude of zero degrees pitch and roll, and a Mach number of 0.92, the velocity at which the vehicle experiences the largest $\Delta C_{p,rms}$ levels for this attitude. Figure 8(a) presents the $\Delta C_{p,rms}$ distribution for the simplified forward attachment case, while Fig. 8(b) presents the same data for the detailed FA case. These plots indicate that the region on the Core in the vicinity of the FA experiences the largest fluctuating pressures, regardless of the FA geometry. A comparison of Figs. 8(a) and (b) indicates that the area affected by elevated fluctuating pressure (identified by light blue through red color range) has decreased for the detailed FA geometry case. This observation is confirmed by Fig. 8(c) which presents the difference between the detailed and simplified cases (detailed FA geometry $\Delta C_{p,rms}$ minus simplified FA geometry $\Delta C_{p,rms}$). Note that the area affected by elevated fluctuating pressure should not be confused with the localized increase in the fluctuating pressure also visible in Fig. 8. While the local increases in $\Delta C_{p,rms}$ would tend to increase the amplitude of BFFs, this potential amplitude increase is more than offset by the reduction of the area affected by elevated $\Delta C_{p,rms}$ values, resulting in an overall decrease in the BFFs.

Further insight into the unsteady aerodynamic environment in the vicinity of the FA can be gleaned by examining the power spectral densities (PSDs) and cross-PSDs of pressure time histories measured in this region. Figure 9(a)–(d) presents the PSDs of pressures measured by transducers located at station 25 (see Fig. 1) at 45°, 135°, 225°, and 315° azimuth angles. All four transducers indicate the same trend as a function of FA geometry; changing from the

simplified to detailed FA geometry increases the frequency of the dominant aerodynamic phenomena, while the amplitude of the signal is reduced.

The cross-PSDs of these transducers with transducers at station 25, at 45° and 315° azimuth, are presented in Figs. 10 and 11, respectively. The data presented in red is for the simplified FA, while the detailed FA data is presented in blue. For clarity, the phase data for both cases are plotted on separate graphs. Figures 10(a) and (b) and 11(c) and (d) indicate that the unsteady pressures measured on either side of the FA are closely related. The phase of these cross PSDs at frequencies near PSD peaks is approximately 180°, and the amplitude is similar compared to the PSDs in Figs. 9(a)–(d). Conversely, there appears to be no or very limited interaction between the aerodynamic environments around the two SRBs' forward attachments. The cross-PSDs of pressures measured on one side of the vehicle with respect to the other side (Figs. 10(c) and (d) and 11(a) and (b)) have significantly reduced peaks at the dominant frequencies noted in the PSDs (compare with Figs. 9(a) and (d)), and their phase plots do not exhibit any discernable trends nor notable correlation.

While the previously discussed transducers measured high levels of fluctuating pressures, the largest fluctuating pressures generally occur directly downstream of the FA. Figures 9(e) and (f) present the PSDs of the pressure time histories measured directly behind the FA at station 25. The most prominent feature of these PSDs is the dominant peak which occurs at twice the frequency noted in Figs. 9(a)–(d). This doubling of frequency indicates that the transducer is detecting the 180° out-of-phase phenomena occurring on both sides of the SRB. This behavior was predicted using FUN3D CFD analysis, which employed Delayed Detached Eddy Simulation modeling and indicates that the phenomenon is a coupling of a pair of oscillating shocks on either side of the SRB with the wake structure downstream of the SRB forward attachment.[3]

The Core also experiences large pressure fluctuations just downstream of the ICPS (see Figs. 8(a) and (b)). These pressure fluctuations are associated with the shoulder connecting the ICPS to the interstage section of the Core. While significant, these fluctuating pressures are not as severe as those measured just downstream of the FA.

2. SRB Fluctuating Pressures

A comparison of Figs. 5(a) and (c), 2012 test simplified FA, to Figs. 5(d) and (f), 2014 test detailed FA, indicates that higher SRB fluctuating pressure environments exist for the detailed forward attachment geometry case. The 2014 test simplified geometry data were not used due to the very limited data set acquired. To determine the cause of this difference, a comparison of the time histories acquired at the same model locations for the 2012 simplified geometry, 2014 simplified geometry, and the 2014 detailed geometry were made at matching test conditions. The results (not presented) indicate nearly identical rms levels and time history characteristics for all three cases at locations where similitude would be expected. This observation points to the finer transducer distribution and more detailed test matrix in the 2014 test being the primary source of the apparent increase in fluctuating pressure levels.

For the majority of the flight conditions tested, the highest fluctuating pressures acting on both SRBs occur aft of the forward attachment, as shown in Figs. 6(a), (c), (d), and (f). For a majority of the test conditions, these high fluctuating pressures are measured on the sides of the SRBs facing the Core. This observation is hinted at in Fig. 8, where the $\Delta C_{p,rms}$ is mapped onto the surface of the 3D vehicle model for a flight condition of Mach 0.92, $\alpha = 0°$, $\phi = 0°$. In this figure, the elevated $\Delta C_{p,rms}$ are visible aft of the FA on a portion of the right SRB, most of which is obstructed by the Core component of the vehicle.

At a Mach number of 0.88, the maximum pressure fluctuations occur at the transducers located just aft of the SRB nose-cone/main-body shoulder (station 23 in Fig. 1). At this Mach number, the pressure time histories (presented in Fig. 12) indicate the presence of an alternating flow phenomenon.[4,5] The time histories indicate that the local flow randomly fluctuates between two flow states as it negotiates the turn at the shoulder: a detached subsonic flow and an attached supersonic flow. These two flow states have significantly different mean pressures, resulting in large fluctuations and rms levels. The multiple state-change events noted in Fig. 12 are not representative of the actual launch environment since, unlike a wind tunnel test, the vehicle is continuously accelerating and would only experience a single, or possibly a limited few, state changes as it passes through the critical Mach number.[5]

3. Coherence of Fluctuating Pressures

An initial assessment of the buffet data from the 2012 test indicated the presence of a large region of highly coherent flow on the SLS Core just downstream of the SRB forward attachment. Since coherence is employed in the BFF development process[2], assessing the coherence in this critical region of the vehicle provides further insight into the buffet environment. The influence of FA geometry on the maximum coherence length, L_c, is presented in Fig. 7. In this figure, L_c is presented as a function of Mach number and absolute model pitch angle. Replacing the simplified FA with the detailed FA results in an approximately 50 percent reduction in the maximum coherence length throughout the entire test envelope (compare same conditions in Figs. 7(a) and (b)).

American Institute of Aeronautics and Astronautics

The mean coherence between the pressure time history measured at station 25, 45° azimuth, and pressure time histories measured at all other locations on the vehicle are mapped to the surface of the SLS model and presented in Fig. 13. Figure 13(a) presents the mean coherence when the simplified FA is installed. Compared to the detailed FA geometry (Fig. 13(b)), the highly coherent flow region on the Core is larger, both in the azimuthal and longitudinal direction. This observation is more clearly visible in Fig. 13(c), which shows the difference in coherence between the detailed and the simplified geometry. The mean coherence is lower over a large region of the Core with the detailed FA installed, as indicated by blue regions on the surface of the vehicle.

B. Effect of Fence BMOs

The effect of the three fence variants on the fluctuating pressure environment was assessed. The first two variants consisted of identical fences attached to the boosters on either side of the FA. The first SRB fence variant has a sharp nose while the other SRB fence has a blunt nose (see Fig. 3(a) and (b)). The sharp fence was slightly longer, and both fences were attached at the same azimuthal location on the SRBs. The third fence variant was attached to the Core at an azimuthal location such that the same spacing between the FA and the fences was maintained. This fence configuration exhibits a leading edge similar to the sharp SRB fence but is longer than either of the SRB fences (see Fig. 3(c)). All three fence variants were tested with the detailed FA geometry, and all results will be compared to the baseline SLS-10005 configuration (detailed FA geometry).

1. Fluctuating Pressures

The maximum $\Delta C_{p,rms}$ as a function of Mach number and absolute model pitch angle for each fence BMO variant is presented in Fig. 14. Figure 15 presents the location where the maximum $\Delta C_{p,rms}$ values were measured (corresponding to Fig. 14). Comparing $\Delta C_{p,rms}$ levels of the three fence variants to the baseline case (detailed FA installed), Fig. 5(d)–(f), indicates a significant reduction in $\Delta C_{p,rms}$ levels throughout the entire test matrix. Although using the same color intensity scale as Fig. 5 masks some subtle differences, Fig. 14 indicates that there is a general insensitivity of the fluctuating pressure rms levels to the fence geometry. This observation holds even if a more refined scale is used (not presented).

A comparison of Figs. 14(b), (e), and (h) indicates that the sharp SRB fence provides a slight benefit compared to the other fences in reducing the Core $\Delta C_{p,rms}$ levels over a large range of test conditions, but beyond this subtle difference, the three fence variants work almost identically. One of the major changes to the maximum $\Delta C_{p,rms}$ levels that the fences introduce is a decrease in the Mach number at which the maximum fluctuating pressures are measured. For the baseline configuration (Fig. 5(e)), the highest $\Delta C_{p,rms}$ levels occurred in a Mach number range of 0.92 to 0.96. With the fences installed, this Mach number range shifted to 0.86 to 0.90 regardless of the fence installed. This reduction in Mach number provides the benefit of a decrease in the dynamic pressure at which peak fluctuations occur in addition to lower $\Delta C_{p,rms}$ levels.

The introduction of the fences also had an impact on the location where the maximum fluctuation pressure environment was measured. The fence-produced changes in the aerodynamic environment near the FA affected the location on the Core where maximum $\Delta C_{p,rms}$ occurred. Without fences, the maximum $\Delta C_{p,rms}$ levels occurred strictly behind the SRB forward attachments (as presented in Fig. 6(e)), but the addition of the fences reduced the fluctuation pressures near the FA such that other regions of the Core susceptible to large pressure fluctuations are highlighted. For the sharp SRB fence, these include terminal shocks on the MPCV near $M = 0.9$, a phenomenon involving the LAS nozzle wake near $M = 1.1$, and unsteadiness associated with the expansion corner created by the ICPS/Core-body junction (see Fig. 15(b)). Similar unsteady pressure results can be noted for the other fence variants (see Figs. 15(e) and (h)).

The unsteady pressure environment measured on the boosters is altered by the fences in a manner similar to the Core, as observed by comparing Figs. 5(d) and (f) to Figs. 14(a) and (c), (d) and (f), and (g) and (i). As previously noted for the Core, the Mach number range at which the highest values of $\Delta C_{p,rms}$ occur shifts to a lower range, Mach 0.85 to 0.90. Similarly, the maximum fluctuating pressures measured on the SRBs are reduced throughout the entire test envelope.

With the reduction in unsteady pressure near the FA, unsteady pressures acting on other areas of the SRBs become more prominent. Figures 15(a), (c), (d), (f), (g), and (i) indicate that the new region of high $\Delta C_{p,rms}$ occurring at lower Mach numbers (noted above and visible in Figs. 14(a) and (c), (d) and (f), and (g) and (i)) is associated with fluctuating pressures measured just downstream of the SRB-nose-cone/main-body shoulder. An examination of the pressure time histories acquired by these transducers (not presented) indicates that the large fluctuations are produced either by a bi-modal flow phenomenon previously discussed in Section III.A.2, or an oscillating shock wave.

The other area of large fluctuations in pressure is the aft skirt of each SRB. Here the aerodynamic environment is affected by large stiffening rings and numerous protuberances located in this region. The fluctuating pressure measured in these regions are generally unaffected by the presence of the fences (not presented).

2. Coherence of Fluctuating Pressures

The effect of the fences on the maximum coherence lengths determined for the segment of the Core downstream of the FA (highlighted in Fig. 1) can be determined by comparing Fig. 7(b) and 16(a)–(c). All three fence variants significantly reduce the coherence length in this region of the vehicle—a beneficial trend since a reduction in the coherence of the flow reduces the magnitude of the forcing functions developed using these pressures.[2]

C. Effect of Nose Cone BMOs

The effect of three SRB nose cone variants on the fluctuating pressure environment was assessed. The geometries of these nose cones are presented in Fig. 4. The tips of all three modified nose cones initiate at the same vehicle station as the original nose cone design, but unlike the original design where the nose cone tip is coincident with the centerline axis of the SRB, the tips of the modified nose cone are offset from the SRB centerline axis to a location closer to the Core body. These nose cones also share the additional feature that the inward side of the nose cones maintain a constant distance from the SLS Core. Figure 4(a) presents the first nose cone. It is referred to as a canted straight nose cone because it is a modified baseline nose cone where the longitudinal axis of the cone is canted towards the SLS Core. The second nose cone is a canted ogive, presented in Fig. 4(b), where the radius of the nose cone changes as a smooth polynomial function. This shape was developed to alleviate the potential of significant fluctuating pressure at the expansion corner located on the outward side of the SRB. The last nose cone variant tested was the bent biconic nose cone (Fig. 4(c)). This nose cone is made of two conical regions developed to approximate the canted ogive shape, but address potential manufacturability difficulties of the ogive nose cone. The fluctuating pressure measurements of these three variants, with the detailed FA installed, will be compared to the results of the baseline nose cone with the detailed FA installed.

1. Fluctuating Pressures

Plots of the maximum $\Delta C_{p,rms}$ as a function of Mach number and absolute model pitch angle for each nose cone variant are presented in Fig. 17. Figure 18 presents the location of the maximum $\Delta C_{p,rms}$ as a function of Mach and absolute model pitch angle, corresponding to Fig. 17

The maximum $\Delta C_{p,rms}$ levels measured on the SLS Core as a function of test conditions for the canted straight nose cones is presented in Fig. 17(b). Compared to the baseline configuration (Fig. 5(e)), the modified nose cone helped reduce the maximum fluctuating pressure environment throughout the test envelope, but the reductions are not as dramatic as those produced by the fence BMOs. There is still an increased $\Delta C_{p,rms}$ region between Mach 0.9 and 0.95, but at low pitch angles the pressure fluctuations are now small.

The locations of the maximum $\Delta C_{p,rms}$ on the Core with the canted straight SRB nose cones installed are presented in Fig. 18b. For the majority of the test conditions, the maximum pressure fluctuations are still observed near the FA, although the $\Delta C_{p,rms}$ reductions achieved through the use of the canted straight nose cones bring to prominence some of the phenomena previously observed for the fence configurations: terminal shocks, LAS wakes, etc. as discussed in Section III.B.1.

The maximum $\Delta C_{p,rms}$ levels measured on the SRBs with the canted straight nose cones installed are provided in Figs.17(a) and (c). A Mach number region between Mach 0.9 and 0.95 still exists where the fluctuating pressures are the highest. At low model pitch angles, this large fluctuating pressure was identified as an alternating flow phenomenon occurring on the outboard half of the SRB (away from the Core). At this location, the nose cone angle (i.e., the angle of the expansion corner) is the largest due to the canted centerline of its design. The large jumps in pressure associated with the two flow states (not presented, but a representative time history can be found in Fig. 12) (subsonic detached and supersonic attached) can be seen as far back as station 24. In fact, station 24 on the right SRB measures the most severe fluctuating pressure environment, which is reflected by differences in the maximum $\Delta C_{p,rms}$ location plots at Mach 0.9, $\alpha = 0°$ (see Figs. 18(a) and (c)). At most other conditions, the maximum fluctuation pressures are found primarily just downstream of the FA.

The second nose cone variant tested was the canted ogive. Figure 17(e) presents the maximum $\Delta C_{p,rms}$ levels measured on the Core as a function of Mach number and absolute model pitch angle. Qualitatively, this nose cone design performs better than the canted straight design. This nose cone design reduces the maximum fluctuation pressures measured on the Core throughout most of the flight envelope, with the exception of the large model pitch angles at Mach conditions above the speed of sound. These relatively high angle test conditions are outside the nominal flight envelope and therefore are not a serious concern. As noted for the canted straight design, the decrease

in fluctuating pressure levels near the FA brought the terminal shock on the MPCV at Mach 0.9 and unsteadiness associated with the LAS nozzles (Fig. 18(e)) to prominence.

The biggest difference in the fluctuating pressure environment attributed to the two nose cone designs is measured on the SRBs. The canted ogive design experiences lower fluctuating pressures on the SRBs at subsonic speeds, but slightly greater fluctuating pressures at supersonic speeds (compare Figs. 17(d) and (f) to Figs. 17(a) and (c)). This difference can be explained by examining the locations where the maximum fluctuation pressures are measured. A comparison of Figs. 18(d) and (f) to Figs. 18(a) and (c) indicates that for the ogive nose cone design, the maximum $\Delta C_{p,rms}$ levels are now measured on the nose cones for a large portion of the flight conditions. Further analysis (not presented) determined that the transducers measuring these large fluctuation pressures face the Core and are measuring the unsteady flow environment in the gap between the Core and the SRB.

The final nose cone design examined in this study was the bent biconic nose cone (Fig. 4(c)). The maximum $\Delta C_{p,rms}$ levels measured on the Core for this nose cone design are significantly lower than the baseline (Fig. 5(e)) and are very similar in magnitude and location to the ogive design (compare Fig. 17(h) to 17(e) and Fig. 18(h) to 18(e)). The SRB fluctuating pressure levels of the bent biconic design, while an improvement over the baseline design, are worse than the ogive at subsonic conditions (compare Figs. 17(g) and (i) to 17(d) and (f)). These large pressure fluctuations at subsonic conditions were measured on the nose cone, as noted in Figs. 18(g) and (i). Almost exclusively, these large $\Delta C_{p,rms}$ levels are located at a transducer station located just downstream of the joint between the two conic segments of the bent biconic nose cones.

2. Coherence of Fluctuating Pressures

Coherence lengths were determined for the segment of the Core downstream of the FA (highlighted in Fig. 1) for all three nose cone variants. In general, all three nose cones affected the fluctuating pressure environment such that the coherence lengths were reduced throughout the flight conditions tested (compare Fig. 7(b) and Figs. 19(a)–(c)). As was the case with the maximum $\Delta C_{p,rms}$ values, the worst performing nose cone was the canted straight nose cone. At high model pitch angles in a Mach number range of 0.9 to 0.95, the coherence lengths for the canted straight nose cone variant were substantially higher than the ogive or bent biconic nose cones. The ogive and bent biconic nose cones had a similar effect on the coherence lengths throughout the entire flight envelope tested.

IV. Conclusions

A transonic buffet wind-tunnel test program was conducted for the Space Launch System launch vehicle. The test program identified a region of large fluctuating pressures whose unsteadiness is linked to the multibody configuration of the SLS vehicle and the geometry of the forward attachment connecting the solid rocket boosters to the center body of the vehicle, or Core. Two parameters were employed to provide an initial assessment of the unsteady pressure environment acting on this vehicle: the coefficient of the root-mean-square fluctuation of pressure about the mean and coherence length of the flow on the segment of the Core just down stream of the forward attachment point of the SRBs. The following conclusions can be inferred from the analyzed wind-tunnel test data:

- The fluctuating pressure environment is extremely sensitive to the SRB forward attachment geometry. Unsteady pressures can be reduced significantly by geometric changes to the forward attachment. These changes can reduce the coherence length by 50 percent or more.

- The addition of flow fences on either side of the SRB forward attachment can significantly reduce the unsteady pressure environment, as well as the coherence lengths, for all flight conditions tested. Attachment of fences to either the SRBs or the Core provided similar reductions in fluctuating pressures, and changes in the fence leading edge produced minor differences in the two parameters examined.

- Changes in SRB nose cones also reduced the unsteady pressure environment and coherence lengths compared to the baseline SLS configuration. The nose cones were slightly less effective than the fences at reducing the fluctuating pressure environment. Test data indicates that at high subsonic Mach numbers, the canted straight nose cone design performed significantly worse than other nose cone options.

References

[1] Piatak, D. J., Sekula, M. K., Rausch, R., Florence, J. R., Ivanco, T. G., "Space Launch System Transonic Buffet Environment Test Program Overview," *53rd AIAA Aerospace Sciences Meeting*, Kissimmee, FL, 2014.

[2] Piatak, D. J., et al., "Data Analysis and Results Document for the 3.5 Percent Ares I Rigid Buffet Model," ARES-AE-TA-0013, July 2009.

[3] Brauckmann, G. J., Alter, S. J, Kleb, W. L., Streett, C., Glass, C., Murphy, K. J., "Computational and Experimental Fluctuating Pressures on an SLS Configuration with Modified Booster Nose Shapes," *53rd AIAA Aerospace Sciences Meeting*, Kissimmee, FL, 2014.

[4] Chevalier, H. and Robertson J., "Pressure Fluctuations Resulting from an Alternating Flow Separation and Attachment at Transonic Speeds,". AEDC-TDR-63-204, November 1963.

[5] Sekula, M. K., Piatak, D. J, Rausch, R., "Analysis of Ares Crew Launch Vehicle Transonic Alternating Flow Phenomenon," *Journal of Spacecraft and Rockets*, Vol. 49, No. 5, 2012, pp. 788-797. doi: 10.2514/1.A32154
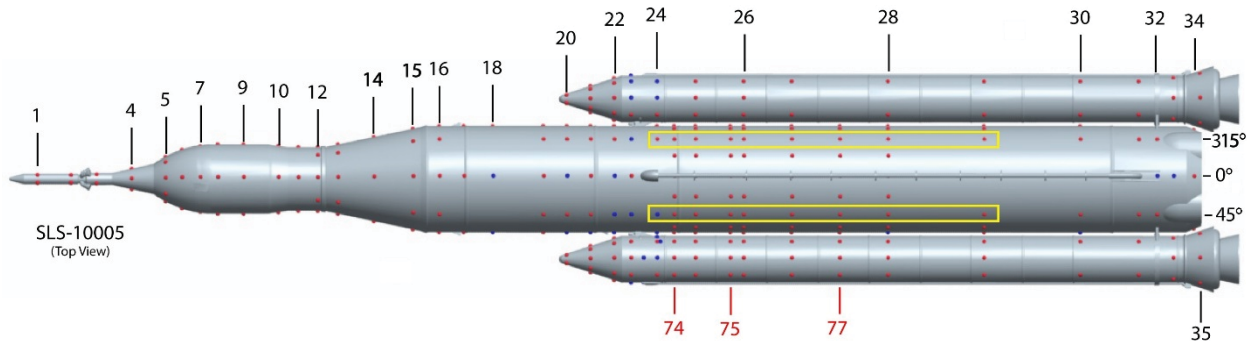
Figure 1. Transducer layout for the SLS-10005 vehicle (additional stations for 2014 test are labeled starting with a "7").
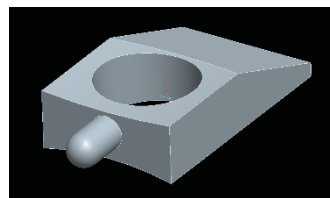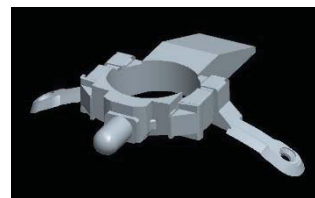
(a) Simplified   (b) Detailed

Figure 2. SRB forward attachment geometries.
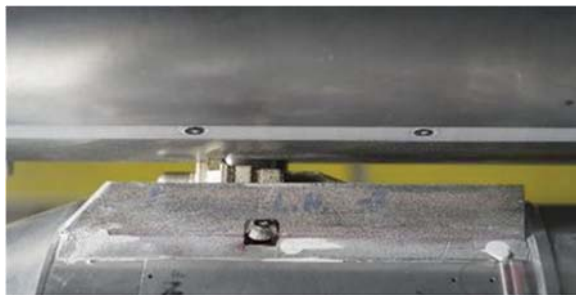
(a) Sharp SRB fence   (b) Blunt SRB fence
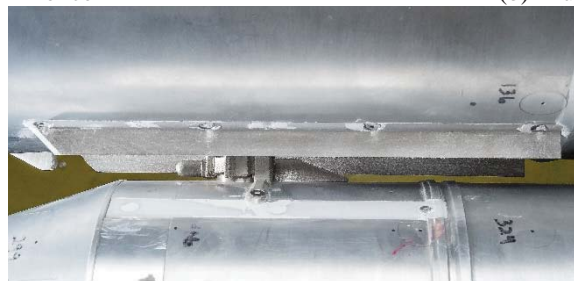
(c) Core fence

Figure 3. Flow fence variants.

| (a) Canted straight | (b) Canted ogive | (c) Bent biconic |
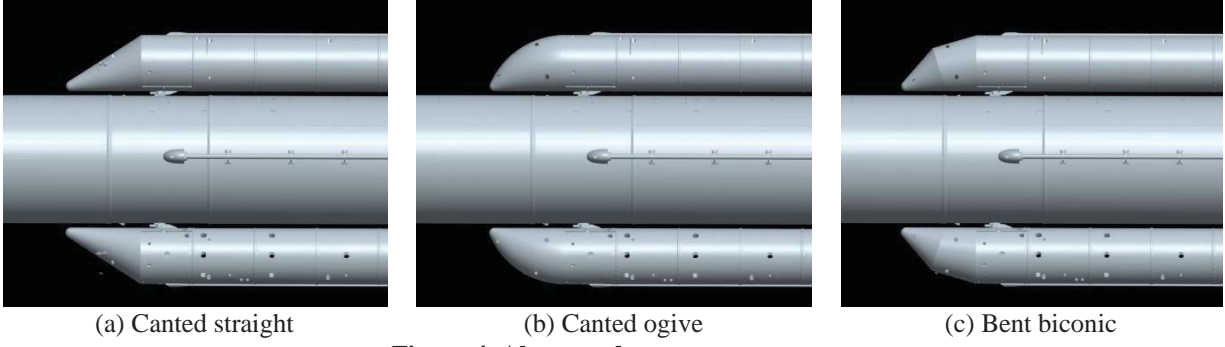
Figure 4. Alternate booster nose cones.

| (a) Left SRB, simplified FA | (b) Core, simplified FA | (c) Right SRB, simplified FA |
| (d) Left SRB, detailed FA | (e) Core, detailed FA | (f) Right SRB, detailed FA |
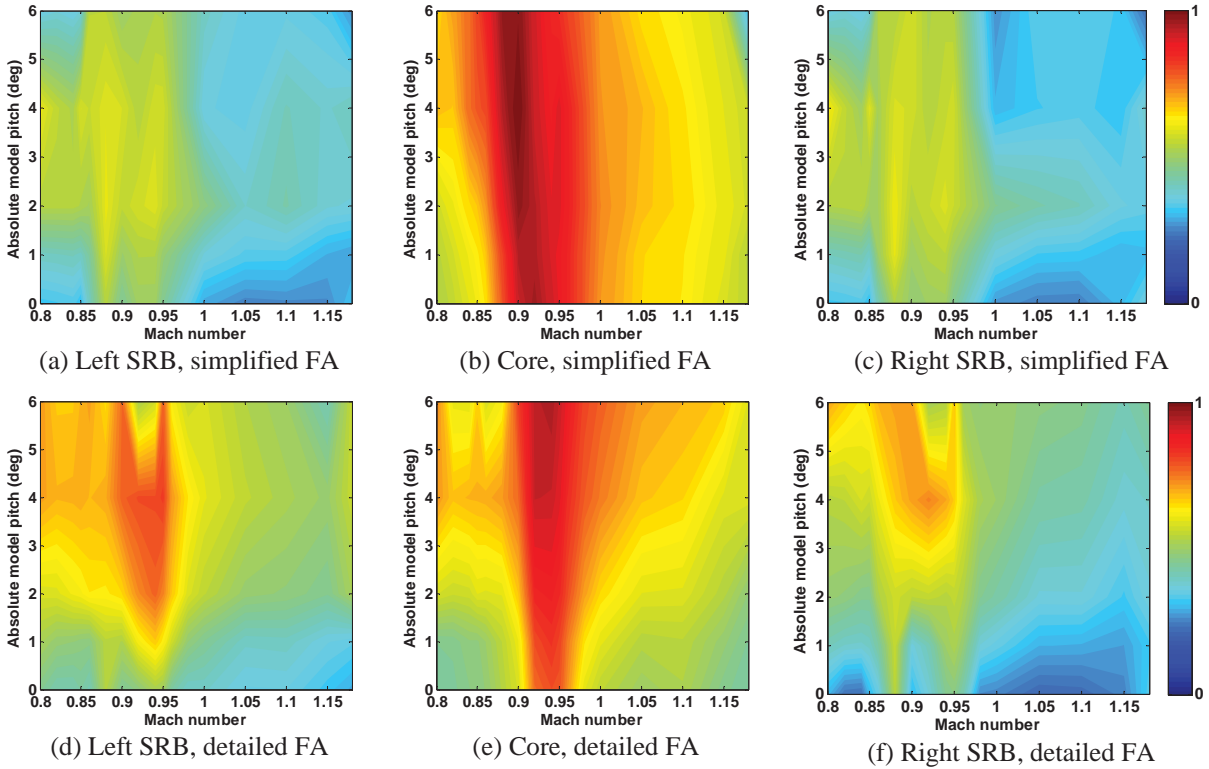
Figure 5. Maximum $\Delta C_{p,rms}$ as a function of Mach and absolute model pitch.
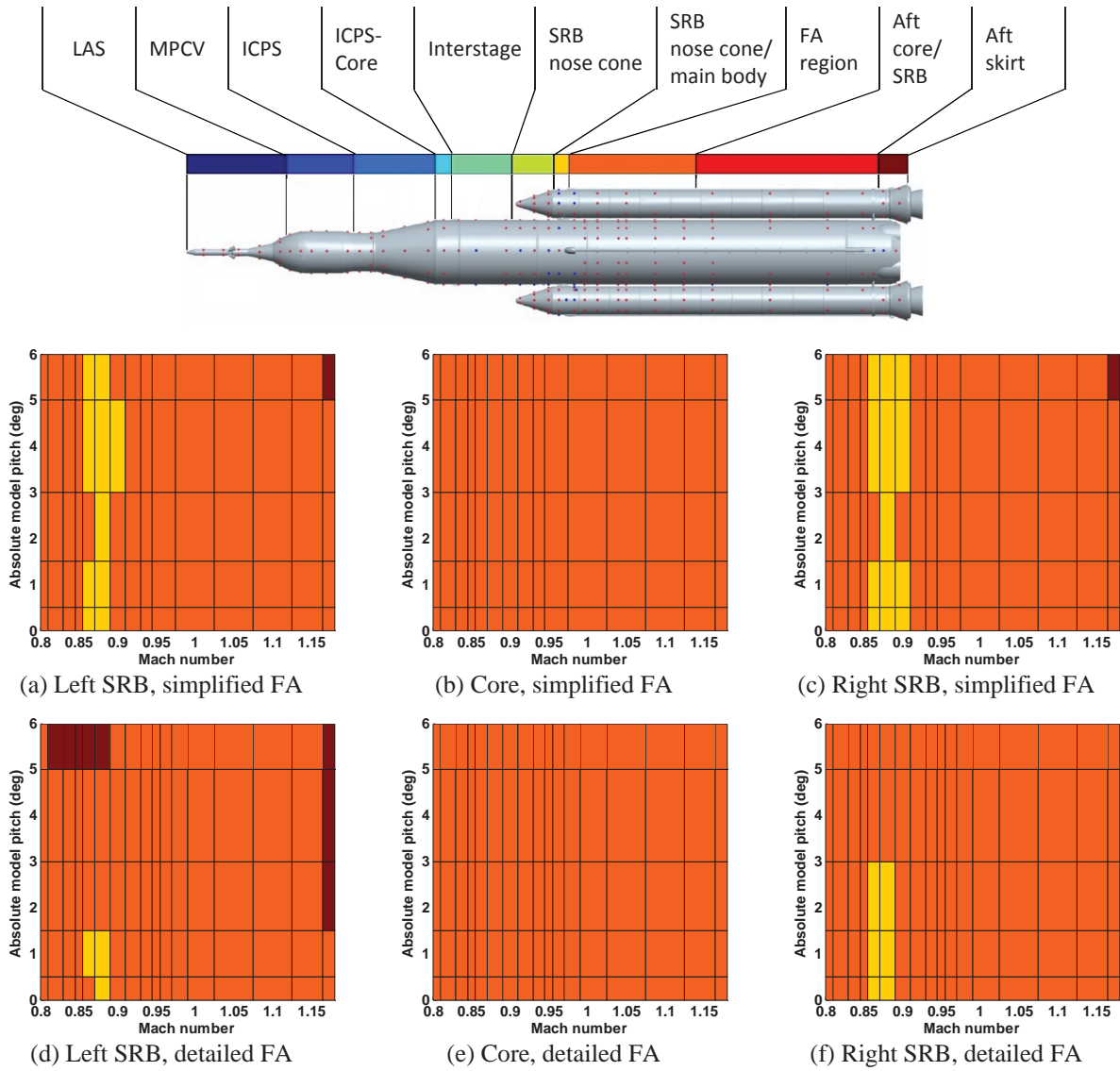
Figure 6. Location of maximum $\Delta C_{p,rms}$ as a function of Mach and absolute model pitch.

(a) Left SRB, simplified FA

(b) Core, simplified FA

(c) Right SRB, simplified FA

(d) Left SRB, detailed FA

(e) Core, detailed FA

(f) Right SRB, detailed FA

(a) Simplified FA geometry

(b) Detailed FA geometry
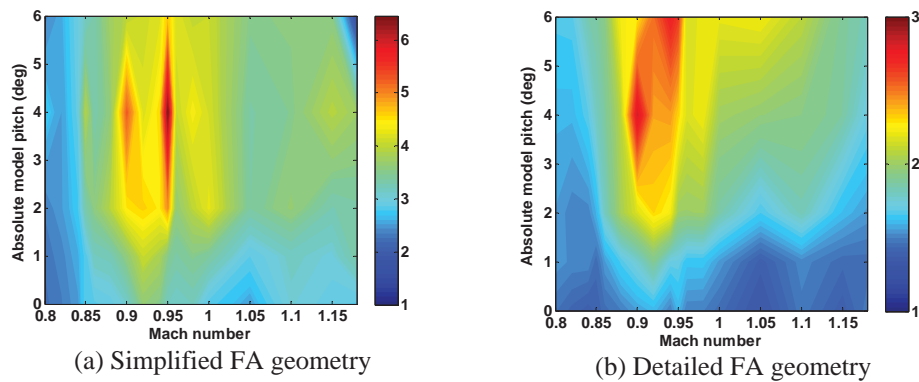
Figure 7. Maximum coherence length, L_c, on the SLS Core as a function of Mach and absolute model pitch.

(a)   Simplified

(b)   Detailed

(c)   Difference (detailed minus simplified)
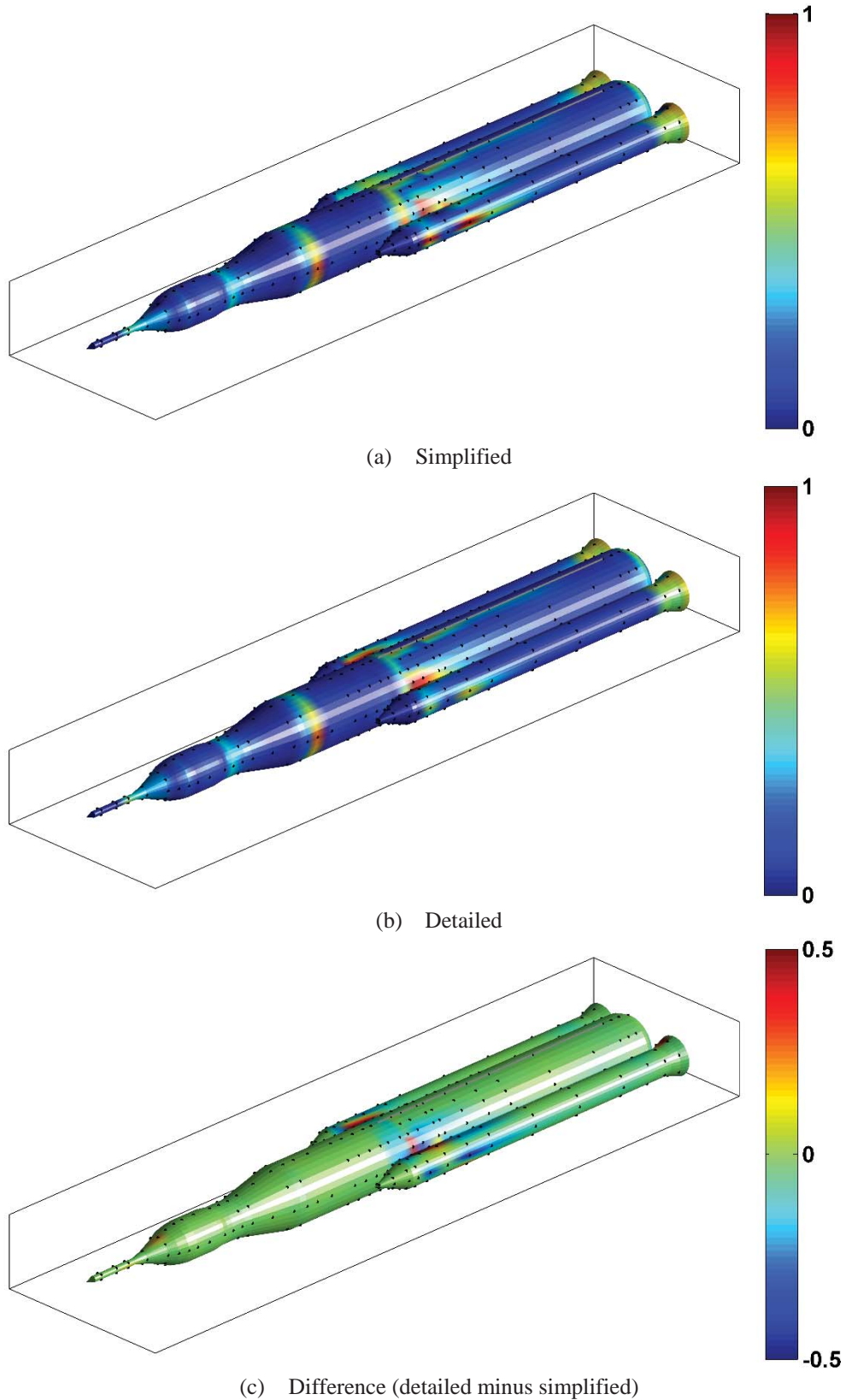
Figure 8. $\Delta C_{p,rms}$ on the surface of the SLS vehicle, $M = 0.92$, $\alpha = 0°$, $\phi = 0°$.

(a) Azimuth 45°

(b) Azimuth 135°

(c) Azimuth 225°

(d) Azimuth 315°

(e) Azimuth 90°
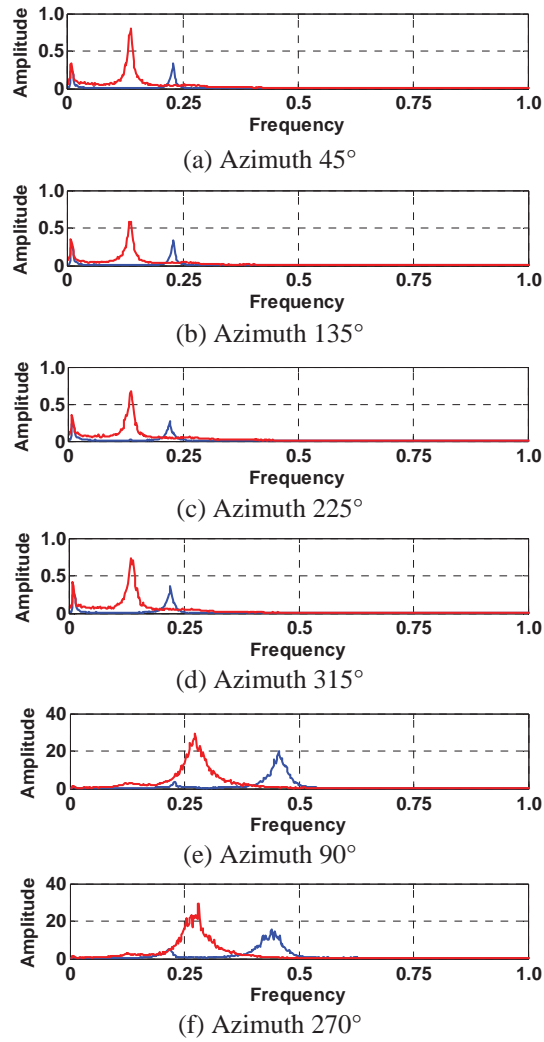
(f) Azimuth 270°

Figure 9. Power spectral density (simplified FA in red, detailed FA in blue), station 25, $M = 0.92$, $\alpha = 0°$, $\phi = 0°$.
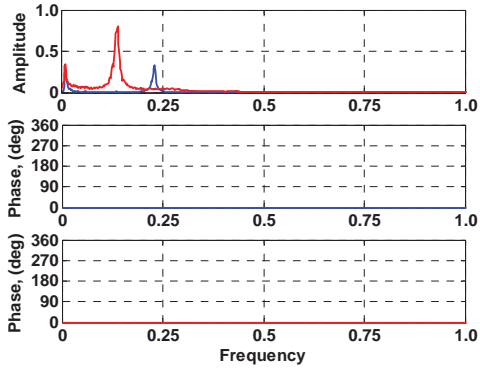
(a) Azimuth 45 – azimuth 45
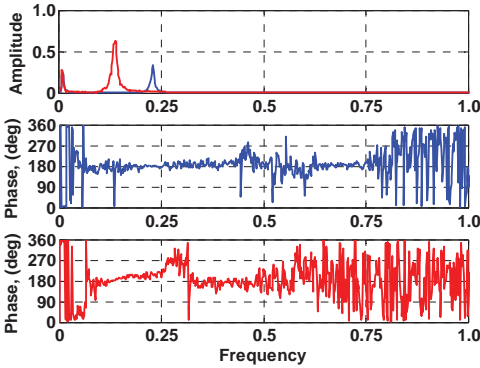
(b) Azimuth 45 – azimuth 135
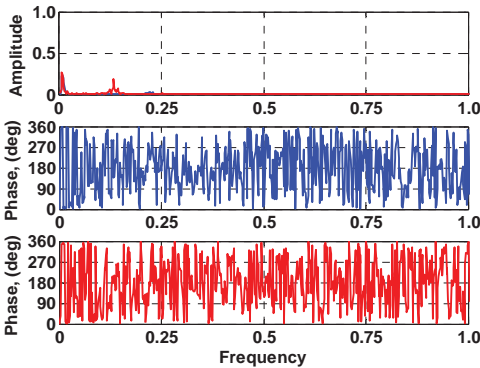
(c) Azimuth 45 – azimuth 225
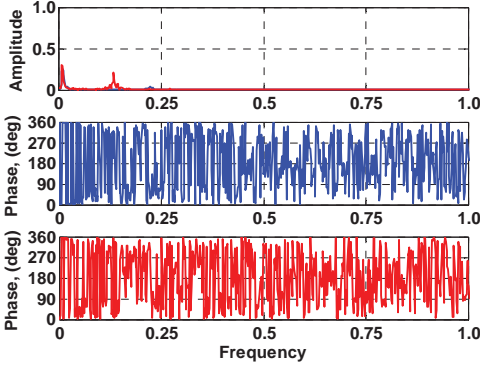
(d) Azimuth 45 – azimuth 315

Figure 10. Cross-PSD with 45° transducer (simplified FA in red, detailed FA in blue), station 25, $M = 0.92$, $\alpha = 0°$, $\phi = 0°$.
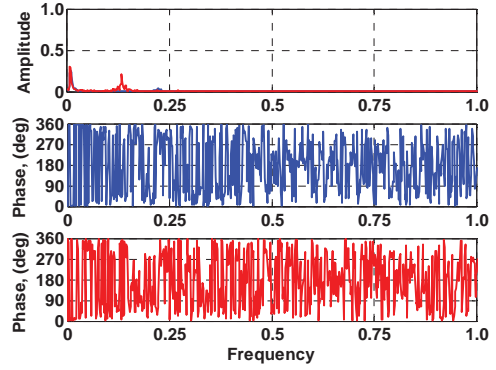
(a) Azimuth 315 – azimuth 45
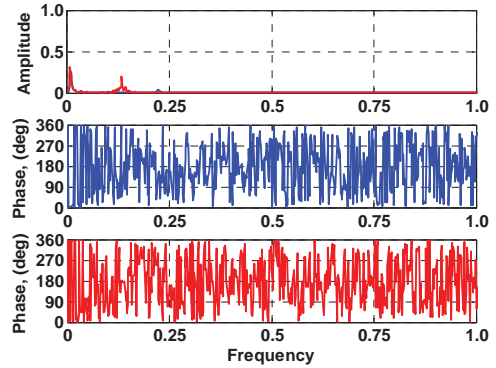
(b) Azimuth 315 – azimuth 135
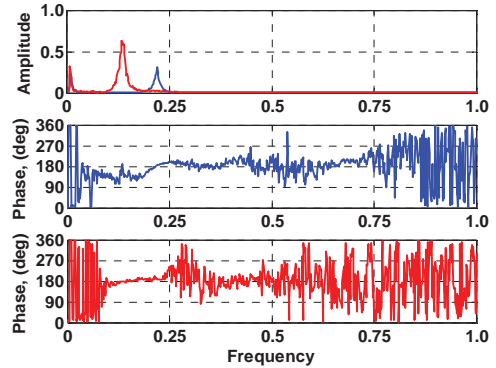
(c) Azimuth315 – azimuth 225
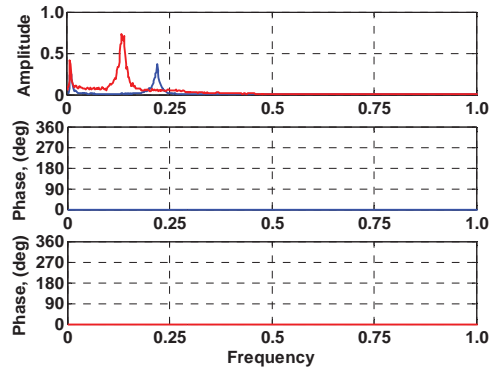
(d) Azimuth315 – azimuth 315

Figure 11. Cross-PSD with 315° transducer (simplified FA in red, detailed FA in blue), station 25, $M = 0.92$, $\alpha = 0°$, $\phi = 0°$.
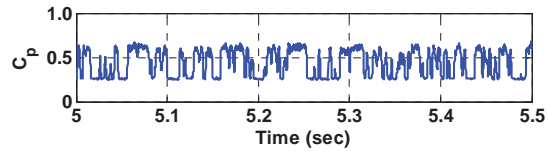
(a) Left SRB, azimuth 45°
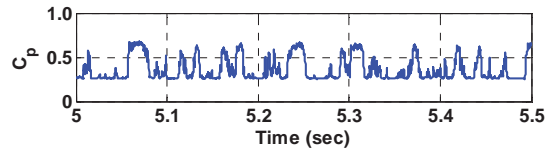
(b) Left SRB, azimuth 135°
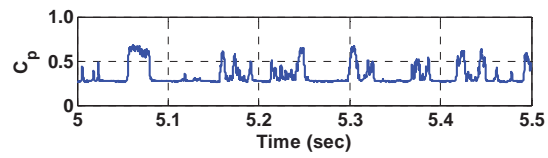
(c) Right SRB, azimuth 270°
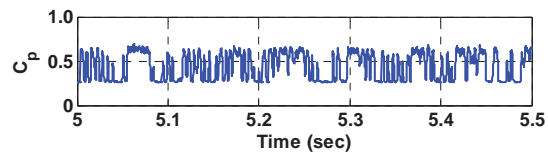
(d) Right SRB, azimuth 315°

Figure 12. Sample alternating flow time histories of left and right SRB, station 23, $M = 0.88$, $\alpha = 2°$, simplified FA geometry, 2012 test.
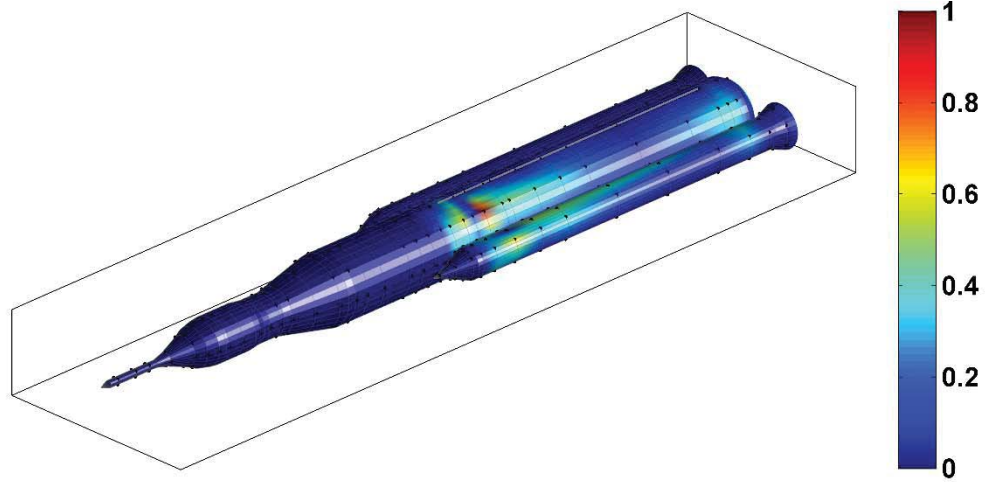
(a) Simplified
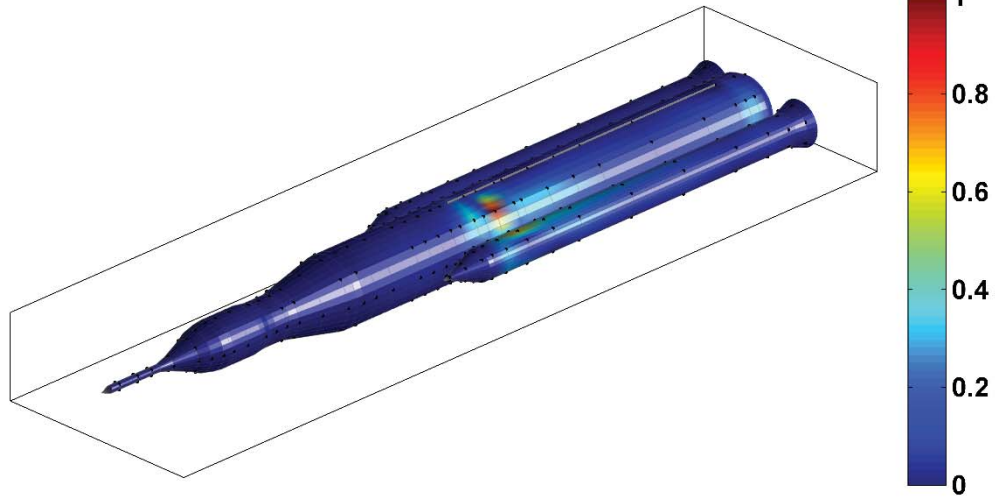
(b) Detailed
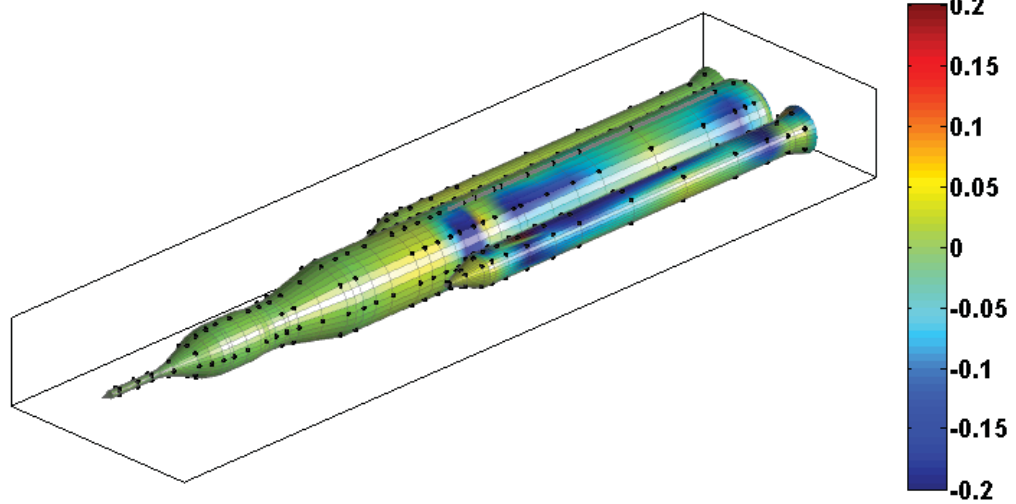
(c) Difference (detailed minus simplified)

Figure 13. Mean coherence with transducer at station 25, azimuth = 45°, $M = 0.92$, $\alpha = 0°$, $\phi = 0°$.

(a) Left SRB, sharp SRB fence   (b) Core, sharp SRB fence   (c) Right SRB, sharp SRB fence
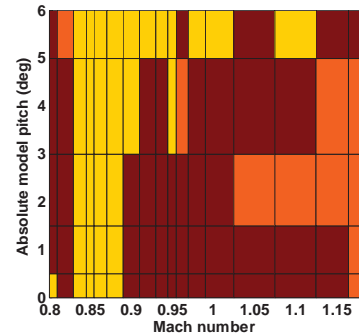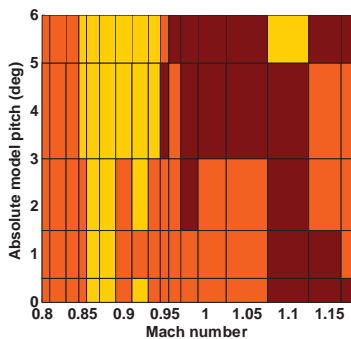
(d) Left SRB, blunt SRB fence   (e) Core, blunt SRB fence   (f) Right SRB, blunt SRB fence
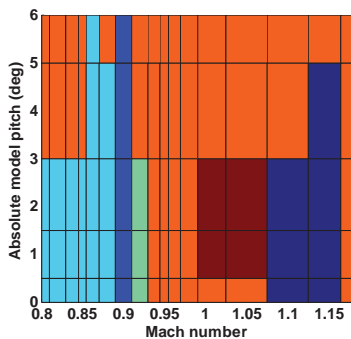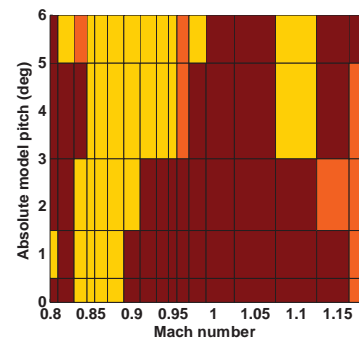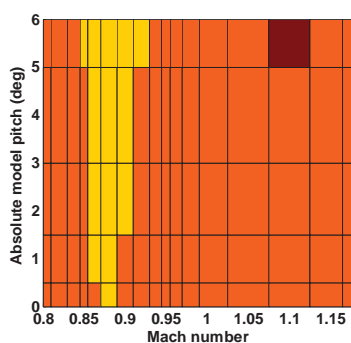
(g) Left SRB, Core fence   (h) Core, Core fence   (i) Right SRB, Core fence
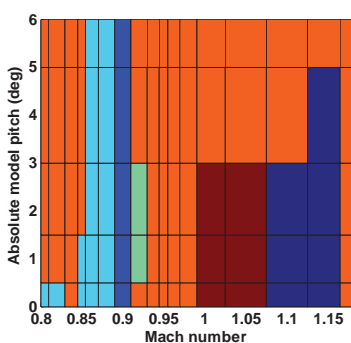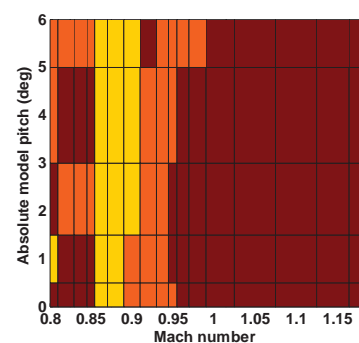
Figure 14. Maximum $\Delta C_{p,rms}$ as a function of Mach and absolute model pitch angle, BMO fence variants.

Figure 15. Location of maximum $\Delta C_{p,rms}$ as a function of Mach and absolute model pitch angle, BMO fence variants.

(a) Sharp SRB fence (b) Blunt SRB fence (c) Core fence
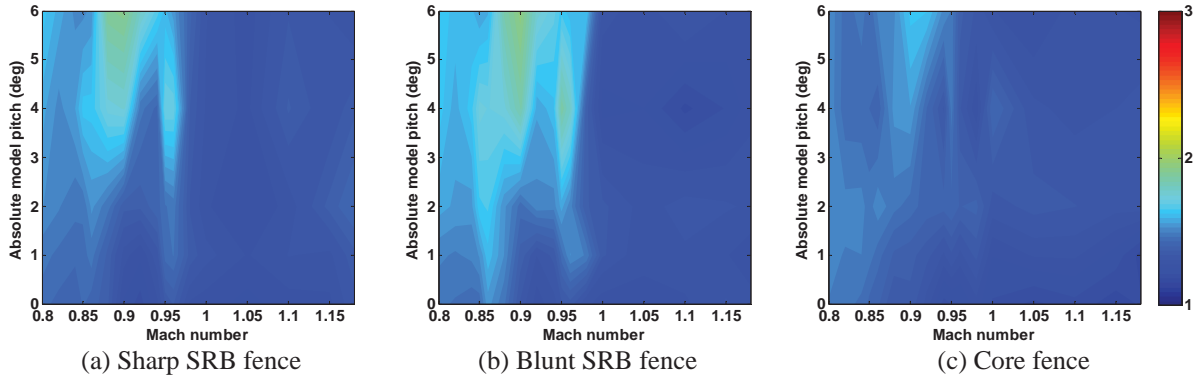
Figure 16. Maximum coherence length, L_c, on SLS Core as a function of Mach and absolute pitch, BMO fence variants.

(a) Left SRB, canted straight (b) Core, canted straight (c) Right SRB, canted straight

(d) Left SRB, canted ogive (e) Core, canted ogive (f) Right SRB, canted ogive

(g) Left SRB, bent biconic (h) Core, bent biconic (i) Right SRB, bent biconic
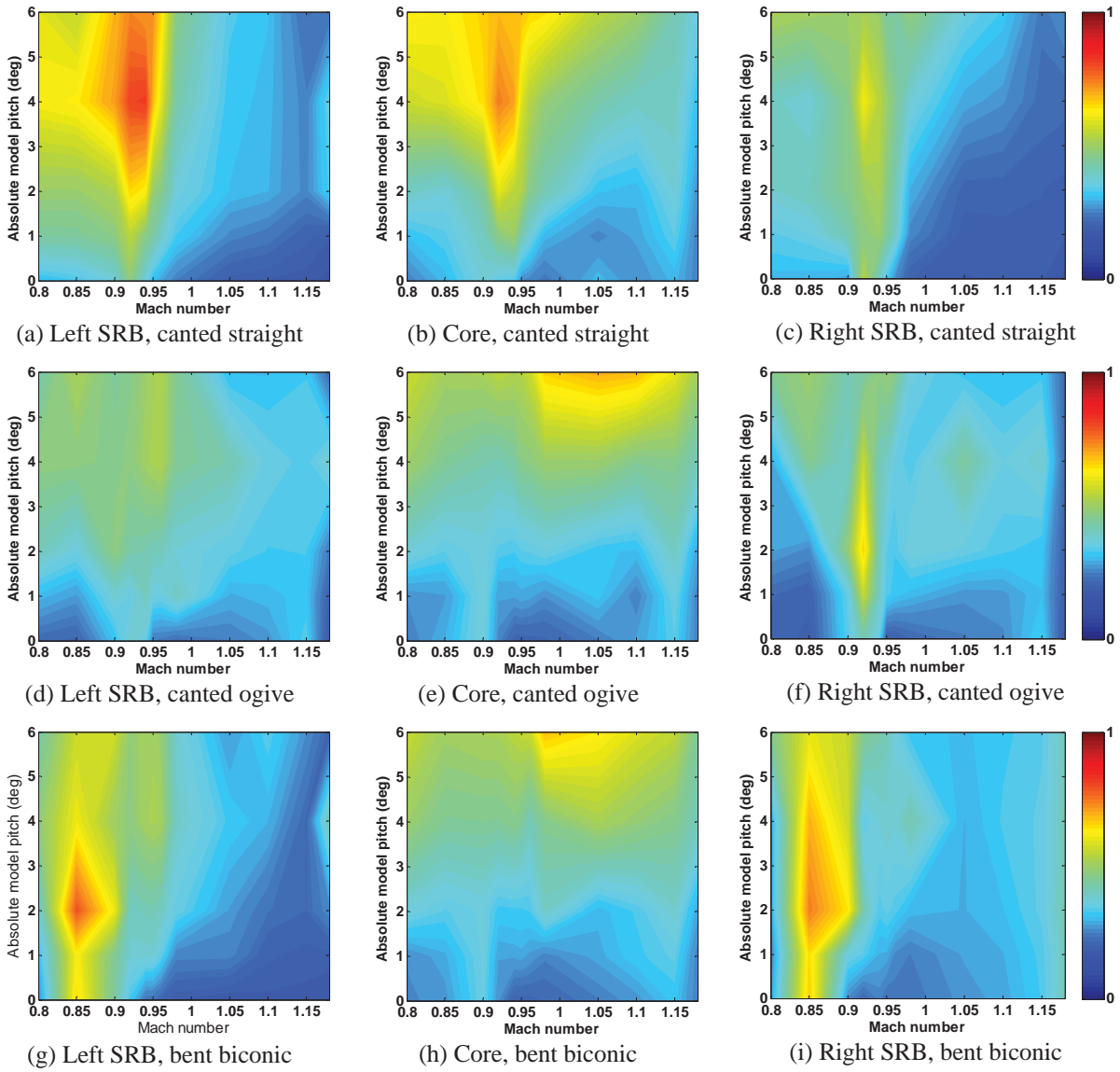
Figure 17. Maximum $\Delta C_{p,rms}$ as a function of Mach and absolute model pitch angle, SRB nose cone variants.
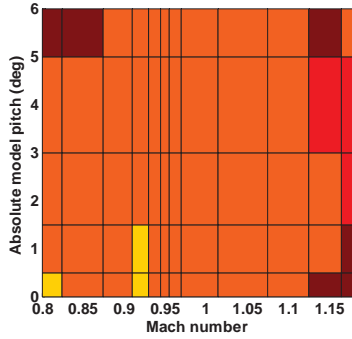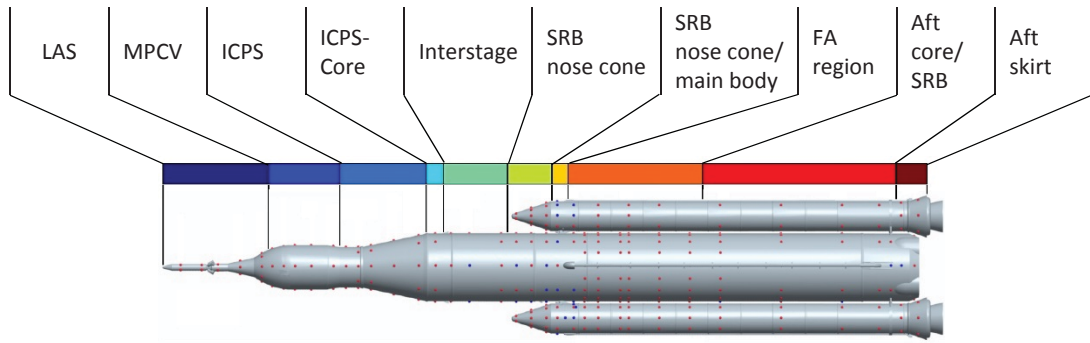
(a) Left SRB, canted straight   (b) Core, canted straight   (c) Right SRB, canted straight
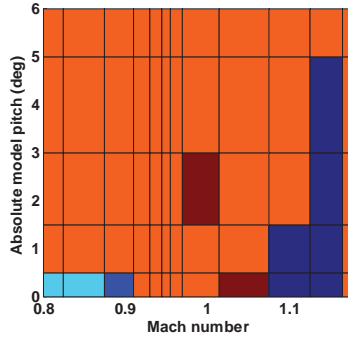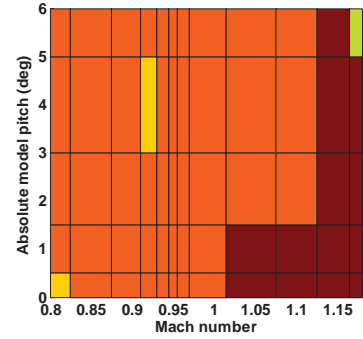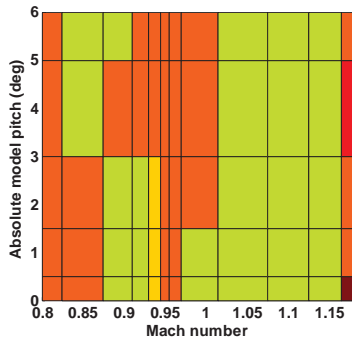
(d) Left SRB, canted ogive   (e) Core, canted ogive   (f) Right SRB, canted ogive
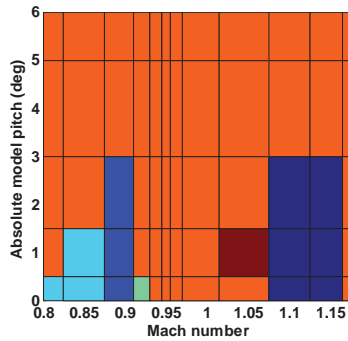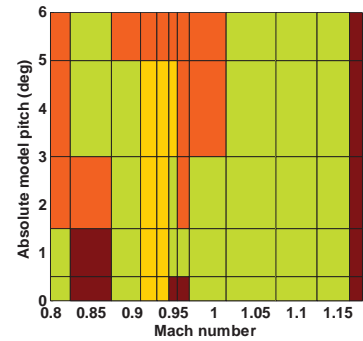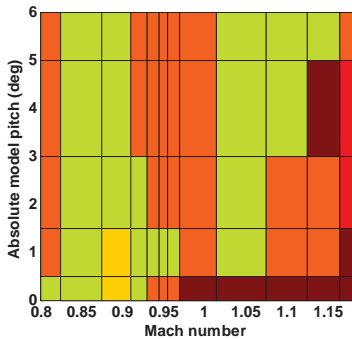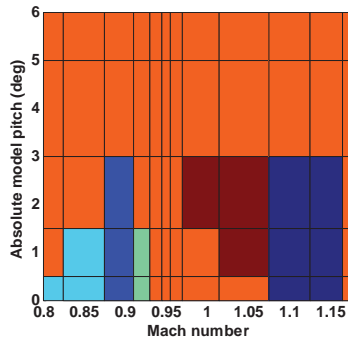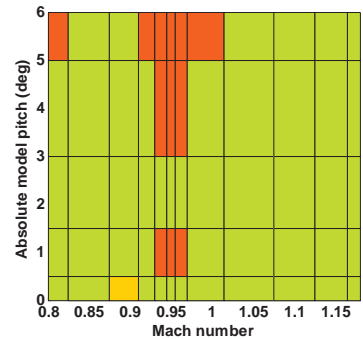
(g) Left SRB, bent biconic   (h) Core, bent biconic   (i) Right SRB, bent biconic

Figure 18. Location of maximum $\Delta C_{p,rms}$ as a function of Mach and absolute model pitch angle, SRB nose cone variants.
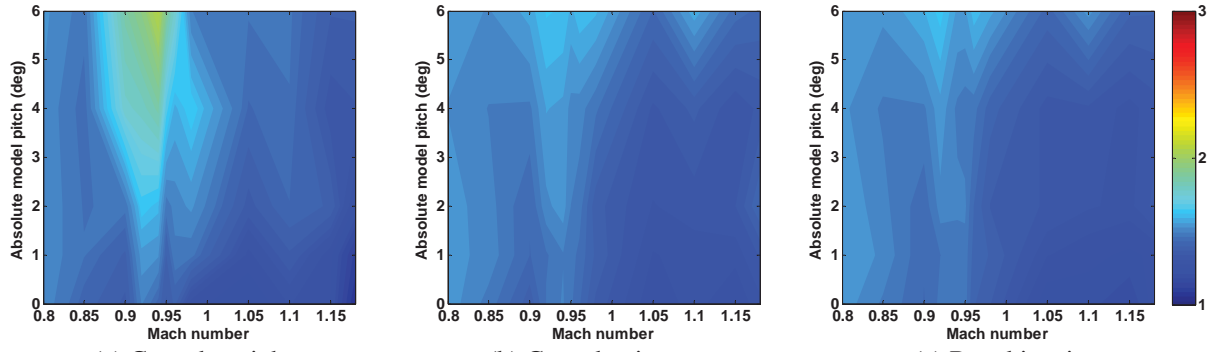
(a) Canted straight   (b) Canted ogive   (c) Bent biconic

Figure 19. Maximum coherence length, L_c, on SLS Core as a function of Mach and absolute model pitch, SRB nose cone variants.